Hydrogen bond symmetrization and high-spin to low-spin transition of ε-FeOOH at the pressure of Earth's lower mantle •

LESLIE INSIXIENGMAY^{1,*} AND LARS STIXRUDE^{1,†}

¹Earth, Planetary, and Space Sciences, University of California, Los Angeles, California 90095, U.S.A.

ABSTRACT

We focus on the ferric end-member of phase H: ε-FeOOH using density functional theory at the PBEsol+U level. At 300 K, we find that ε-FeOOH undergoes a hydrogen bond symmetrization at 37 GPa and a sharp high-spin to low-spin transition at 45 GPa. We find excellent agreement with experimental measurements of the equation of state, lattice parameters, atomic positions, vibrational frequencies, and optical properties as related to the band gap, which we find to be finite and small, decreasing with pressure. The hydrogen bond symmetrization transition is neither first- nor second-order, with no discontinuity in volume or any of the elastic moduli. Computed IR and Raman frequencies and intensities show that vibrational spectroscopy may provide the best opportunity for locating the hydrogen bond symmetrization transition experimentally. We find that ε-FeOOH is highly anisotropic in both longitudinal- and shear-wave velocities at all pressures, with the shear wave velocity varying with propagation and polarization direction by as much as 24% at zero pressure and 43% at 46 GPa. The shear and bulk elastic moduli increase by 18% across the high-spin to low-spin transition.

Keywords: Mantle, density functional theory, phase transitions, symmetrization, high pressure, phonon

Introduction

Water is an important component in the mantle that, even in small concentrations, can greatly affect properties such as the melting temperature and viscosity, and thus thermal evolution. The amount of water stored in the largest part of the mantle, the lower mantle, is still uncertain. This is partly due to the relative inaccessibility of this region, for example, few physical samples from the lower mantle are known, in contrast to the increasing number of diamond inclusions and other samples from the transition zone (Pearson et al. 2014; Tschauner et al. 2018). Our uncertainty about the water content in the lower mantle is also due to a comparative lack of understanding of hydrogen bonding at high pressure: in what phases is water crystallographically stored, and what is the effect of water on physical properties at high pressure?

Water storage may be fundamentally different in the lower mantle than in the transition zone. In the transition zone, copious amounts of water may be stored in nominally anhydrous minerals, including wadsleyite and ringwoodite, which have water storage capacities exceeding 1 wt% (Hirschmann 2006). In the lower mantle, however, the water storage capacity of the major phases (bridgmanite, ferropericlase, davemaoite), while still uncertain, appears not to exceed 1200 ppm (Litasov and Ohtani 2007; Fu et al. 2019; Chen et al. 2020; Liu et al. 2021). If the lower mantle has a water concentration much higher than this, the water must be stored in hydrous phases, i.e., phases in which water is a stoichiometric component.

Phase H is the hydrous phase that is found to be stable in

mantle-like whole rock compositions with excess H₂O (Walter et al. 2015) over most of the lower mantle pressure regime (55–125 GPa). These experiments were limited in not containing iron oxide as a component, but other studies have found stable solid solution of phase H encompassing essentially the entire ternary (Mg,Fe,Al)(Si,Fe,Al)(OOH)₂ (Nishi et al. 2019), complementing studies of binary joins in this compositional space (Ohira et al. 2019, 2021; Satta et al. 2021).

Our focus here is on the ferric end-member of phase H: ε-FeOOH. ε-FeOOH has an orthorhombic structure with P2₁nm space group that is stable on its own composition from 7 GPa (where it transforms from the lower pressure, goethite phase) to 70 GPa, where it transforms to a pyrite-structured phase (Gleason et al. 2008; Nishi et al. 2017; Suzuki 2017; Hu and Liu 2021). The structure is an orthorhombically distorted rutile derivative with edge- and corner-sharing FeO₆ octahedra linked by hydrogen bonds (O-H···O) that are asymmetric at low pressure (Pernet et al. 1975; Bolotina et al. 2008). The anhydrous sub-lattice (arrangement of Fe and O atoms) is identical to the CaCl₂ high-pressure polymorph of stishovite.

Under pressure ε-FeOOH displays rich behavior undergoing two transitions: hydrogen bond symmetrization and a high-spin to low-spin transition. The ε-FeOOH phase thus serves as a model system for studying two transitions that are thought to be important in many mantle phases at high pressure. Hydrogen bond symmetrization occurs in various materials at high pressure, including phase H (Tsuchiya and Mookherjee 2015), phase D (Tsuchiya et al. 2005), and H₂O (Holzapfel 1972; Aoki et al. 1996; Meier et al. 2018). The high-spin to low-spin transition occurs in a wide variety of ferrous and ferric oxides and silicates (Lin et al. 2005; Tsuchiya et al. 2006; Gleason et al. 2008; Badro 2014; Liu et al. 2014; Holmström and Stixrude

^{*} E-mail: insixiengmay@g.ucla.edu

[†] Orcid 0000-0003-3778-2432

Open access: Article available to all readers online.

2015). A unique feature of ϵ -FeOOH is that the two transitions (hydrogen bond symmetrization and high-spin to low-spin transition) are thought to occur at similar pressures, and the nature of possible interaction between these two transitions, i.e., whether one drives the other, is still uncertain (Gleason et al. 2013; Xu et al. 2013; Thompson et al. 2020).

Hydrogen bond symmetrization occurs as the O-O distance of O-H···O decreases while the O-H bond length increases, leading to a linear symmetric O-H-O configuration and promotion of the space group symmetry to *Pnnm*. The symmetrization transition has been widely studied in the Al end-member of phase H (δ -AlOOH) (Tsuchiya et al. 2008; Tsuchiya and Tsuchiya 2009; Sano-Furukawa et al. 2018) and has been predicted to occur in the MgSi end-member (Tsuchiya and Mookherjee 2015; Solomatova et al. 2022). The pressure at which symmetrization occurs in ϵ -FeOOH is uncertain as neutron diffraction studies have not yet been performed on this phase at high pressure, and previous theoretical studies focused on the symmetrically bonded structure (Thompson et al. 2017).

The high-spin to low-spin transition occurs as increasing crystal field splitting on compression causes d-electrons in the e_g manifold to pair up with those in the t_{2g} manifold, yielding a change in the magnetic moment of the Fe^{3+} cation from 5 to 1 μ_B , and a collapse in volume. The high-spin to low-spin transition has been found to occur between 40 and 60 GPa in experimental studies (Gleason et al. 2013; Xu et al. 2013; Thompson et al. 2020). The high-spin to low-spin transition in ϵ -FeOOH has not yet been studied theoretically; part of the reason is that transition metal oxides present a challenge to conventional density functional theory, which tends to underestimate the strong correlation among the d electrons.

Here we explore the behavior of ϵ -FeOOH at high pressure with density functional theory augmented by local electron repulsion that captures the strong correlation (DFT+U). We study both transitions (hydrogen bond symmetrization and high-spin to low-spin) and explore the changes in properties that occur across them. We focus on physical properties that have been previously measured experimentally in this system, including the structure, equation of state, and vibrational frequencies, and on those that may be relevant to geophysical detection of phase H in the lower mantle, including elasticity, and electronic properties.

METHODS

Our calculations are based on density functional theory (DFT), using the projector augmented wave (PAW) method (Kresse and Joubert 1999) as implemented in the Vienna ab initio Simulation Package (VASP) (Kresse and Furthmüller 1996). We use the PBEsol generalized gradient approximation (Perdew et al. 2008), which we have previously shown to yield excellent agreement with experiment in iron-bearing oxides (Holmström and Stixrude 2015). To account for strong correlation, we use the +U method (Anisimov et al. 1997). On the basis of our calculations of the dependence of the spin transition pressure and ontical properties on U-J, our previous results for the value of U-J for divalent iron (Holmström and Stixrude 2015), and expected trends with respect to iron valence state (Mosey et al. 2008), we settled on a value of U-J = 3.2 eV. We use PAW potentials of 14, 1, and 6 valence electrons for Fe, H, and O with core radii of 1.16, 0.37, and 0.82, respectively. We perform spin-polarized simulations where the difference in the number of up-spin and down-spin electrons on each Fe atom is set to the high-spin (5) or low-spin (1) value for both anti-ferromagnetic and ferromagnetic arrangements (Figs. 1a and 1b). We also explored a mixed-spin arrangement in which half of the Fe are high-spin and the other half are low-spin (Fig. 1c). We found that sampling the Brillouin zone using a 4 × 4 × 4 k-point mesh and a basis-set energy cutoff of 1000 eV was sufficient to converge energy and pressure to within 3 meV/atom and 0.1 GPa, respectively. For calculation of the electronic density of states we use the tetrahedron method (Blöchl et al. 1994) and a 20 × 20 × 20 k-point mesh. For phonon calculations, we use a 2 × 2 × 2 supercell and a $2 \times 2 \times 2$ k-point mesh.

We calculate the elastic constants by applying finite strains ε_{kl} to the lattice and computing the resultant stresses σ_{ij} , yielding the components of the elastic constant tensor as $\sigma_{ij} = c_{ijkl}\varepsilon_{kl}$. We choose a strain magnitude of 0.005 and strains (in Voigt notation): ε_1 , ε_2 , ε_3 , and $\varepsilon_4 + \varepsilon_5 + \varepsilon_6$ appropriate for the orthorhombic case (Le Page and Saxe 2002). The isotropic bulk and shear moduli are determined using the Voigt-Reuss-Hill (Hill 1952) measure. We compute single-crystal elastic wave velocities via the Christoffel equation $|c_{ijk}n_jn_i - \rho v^2\delta_{ik}| = 0$ where c_{ijkl} is the single-crystal elastic tensor, n is the propagation direction, ρ is the density, v is the velocity, and δ_{ik} is the Kronecker delta (Musgrave 1970). The eigenvalues yield the elastic wave velocities, and eigenvectors the polarization directions. We fit our theoretical results to the Eulerian finite strain expansion (Stixrude and Lithgow-Bertelloni 2005):

$$c_{ijkl} = (1 + 2f)^{5/2} \{c_{ijkl0} + (3K_0c'_{ijkl0} - 5c_{ijkl0})f + [6K_0c'_{ijkl0} - 14c_{ijkl0} - \frac{3}{2}K_0\delta^{ij}_{ll} (3K'_0 - 16)]f^2\}$$
(1)

where $f = \frac{1}{2}[(V/V_0)^{-2/3} - 1]$, c_{ijkl} is the elastic tensor, the subscript 0 refers to the reference state $(P = 0 \text{ GPa}, T_0 = 300 \text{ K})$, and $\delta_{il}^{il} = -\delta_{il}\delta_{il} - \delta_{il}\delta_{ik} - \delta_{jl}\delta_{ik}$.

We calculate the phonon vibrational frequencies via density functional perturbation theory (DFPT) (Gajdoš et al. 2006). Phonon frequencies and eigenvectors are computed in the harmonic limit from the second-order force constant matrix $\Phi_{\alpha\beta}(jl,j'l')$, the elements of which are the change in the force in the α Cartesian direction acting on atom j in unit cell l, in response to the displacement of atom j' in unit cell l' in the β direction (Wilson et al. 1980). The phonon frequencies are the eigenvalues of the dynamical matrix at a given wavevector q:

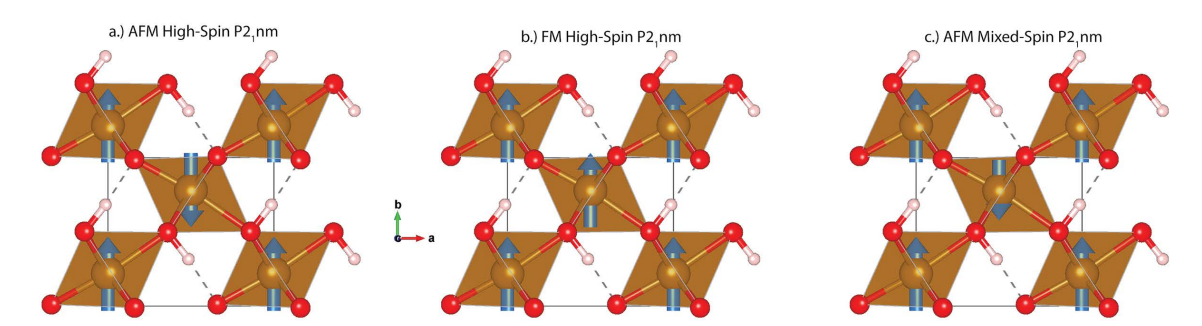


FIGURE 1. The structure of the $P2_1nm$ ε-FeOOH phase in an (a) AFM HS state, (b) FM HS state, and (c) an AFM mixed-spin state. The solid black lines indicate unit cells, oxygen atoms are red spheres, hydrogen atoms are pink spheres, and iron atoms are gold spheres. Blue arrows represent the magnetic moment μ of the iron atoms. The arrow magnitude is related to the spin state (longer = high-spin; shorter = low-spin) and the arrow direction is related to the up/down-spin of valence electrons (up = +μ; down = -μ). Image generated using the software VESTA (Momma and Izumi 2008).

(5)

$$D_{\alpha\beta}^{J'}(\boldsymbol{q}) = \frac{1}{\sqrt{m_j m_{J'}}} \sum_{l'} \Phi_{\alpha\beta}(jl, j'l')$$

$$\exp\left[i\boldsymbol{q} \cdot (\boldsymbol{r}(j', l') - \boldsymbol{r}(j, l))\right]$$
(2)

where m_j are the atomic masses and l and l' are the unit cells of the two atoms.

The long-ranged Coulomb interactions lead to non-analytic corrections in the limit $q \rightarrow 0$, that cause splitting of the longitudinal optic (LO) and transverse optic (TO) modes (Pick et al. 1970; Gonze and Lee 1997):

$$D_{\alpha\beta}^{jj'}\left(q\rightarrow0\right)=D_{\alpha\beta}^{jj'}\left(q=0\right)+\frac{1}{\sqrt{m_{j}m_{j'}}}\frac{4\pi}{\Omega_{0}}\left[\frac{\sum_{\gamma}q_{\gamma}Z_{\gamma\alpha}^{j}}{\sum_{\alpha\beta}q_{\alpha}\varepsilon_{\alpha\beta}^{\alpha}q_{\beta}}\right] (3)$$

where $Z'_{\alpha\beta}$ is the Born effective tensor, ϵ^{ω} is the macroscopic dielectric tensor, and Ω_0 is the volume of the cell.

We compute infrared (IR) intensities from the eigen-displacements around the gamma-point, where the atom's change in polarizability with respect to atomic displacement is captured by the Born effective-charge tensor (Giannozzi and Baroni 1994):

$$I_{IR}(s) = \sum_{\alpha} \left| \sum_{\beta} Z_{\alpha\beta}^{j} \frac{w(s,j)}{\sqrt{m_{j}}} \right|^{2}$$
(4)

where $\mathbf{w}(s,j)$ is the eigenvector of the dynamical matrix corresponding to mode s.

We compute Raman intensities from the change in the polarizability tensor α along the mode eigenvectors in terms of the macroscopic high-frequency dielectric constant (Skelton et al. 2017) via a central finite-difference scheme:

$$\begin{split} I_{\text{Raman}}\left(s\right) & \propto \frac{\partial \alpha}{\partial \mathcal{Q}(s)} \equiv \frac{\partial \varepsilon^{\infty}}{\partial \mathcal{Q}(s)} \approx \frac{\Delta \varepsilon^{\infty}}{\Delta \mathcal{Q}(s)} \\ I_{\text{Raman},\alpha\beta}\left(s\right) & = \frac{\Omega}{4\pi} \left[-\frac{1}{2} \frac{\varepsilon^{\infty}_{\alpha\beta}(-s)}{\Delta \mathcal{Q}(s)} + \frac{1}{2} \frac{\varepsilon^{\infty}_{\alpha\beta}(+s)}{\Delta \mathcal{Q}(s)} \right] \end{split}$$

where Q is the normal-mode coordinate at the Γ -point and is defined by

$$u(s,j) = Q(s) \frac{w(s,j)}{\sqrt{m_s}}$$

where u(s,j) is the atomic displacement. The unpolarized Raman intensity takes the form:

In this.
$$I_{\text{Raman}} = 45 \left[\frac{1}{3} (I_{xx} + I_{yy} + I_{zz}) \right]^2 + \frac{3}{2} \left[(I_{xx} - I_{yy})^2 + (I_{xx} - I_{zz})^2 + (I_{yy} - I_{zz})^2 + (I_{yy} - I_{zz})^2 \right]$$
(6)

To compute phonon frequencies and IR and Raman intensities, we use Phonopy and Phonopy-Spectroscopy (Togo and Tanaka 2015; Skelton et al. 2017).

We find the pressure of the high-spin to low-spin transition as the point at which the Gibbs free energies of the two phases are equal:

$$G(P,T) = H(P,\text{static}) + F_{TH}(V,T) + P(V,T)V, \tag{7}$$

where H is the enthalpy at static (athermal) conditions, G is the Gibbs free energy as a function of pressure P and temperature T, V is the volume, and F_{TH} is the Helmholtz free energy derived from the (quasi-)harmonic phonon energy. The pressure:

$$P(V,T) = P(V,\text{static}) + P_{TH}(V,T), \tag{8}$$

where $P_{TH} = -(\partial F_{TH}/\partial V)_T$

and

$$F_{TH} = \frac{1}{2} \sum_{\alpha i} \hbar \omega_{\alpha i} + k_B T \sum_{\alpha i} \ln\{1 - \exp[-(\hbar \omega_{\alpha i}/k_B T)]\}$$
(9)

where ω is the phonon frequency. We have found that the thermal free energy of the asymmetrically bonded phase is nearly independent of volume, yielding essentially zero thermal pressure. This result is inconsistent with experimental measurements of positive thermal expansivity (Suzuki 2016), indicating that anharmonicity, which is not included at our level of theory, is important in the

asymmetric phase. We hypothesize that the thermal free energy of the asymmetric phase can be approximated by that of the symmetric phase at the same volume. Our hypothesis could be tested by performing molecular dynamics simulations, which are beyond the scope of this study because of the much greater computational cost.

RESULTS

At static conditions, we find that the ground state is high-spin anti-ferromagnetic (AFM), in agreement with a neutron diffraction study at ambient pressure (Pernet et al. 1975) (Fig. 2). The AFM state is more stable than the ferromagnetic (FM) state by 0.5 eV per unit cell (0.25 eV/formula unit) at zero pressure and 0.8 eV at 40 GPa. At 40 GPa, the lowest energy state becomes low-spin AFM. In the low-spin state, AFM is more stable than FM by 0.02 eV at 40 GPa, to 0.01 eV at 100 GPa. We also find that the mixed-spin state is less stable than the high-spin state at 40 GPa by 0.4 eV. Because AFM is the most stable, all subsequent results refer to the AFM arrangement.

We find hydrogen bond symmetrization to occur within the stability field of the high-spin state (Fig. 3). The transition occurs at a static pressure of 34 GPa. The symmetrization transition occurs without discontinuity in structure or volume and is, therefore, not first order. We also show results for the (metastable) symmetrization transition in the low-spin state, which occurs at a static pressure of 5 GPa.

We find excellent agreement with experimental measurements of the equation of state of the high-spin and low-spin states and the pressure of the high-spin to low-spin transition (Suzuki 2010, 2016; Gleason et al. 2013; Ikeda et al. 2019; Thompson et al. 2020) (Fig. 4). We find that the high-spin to low-spin transition occurs at 45 GPa at 300 K. We find disagreement with some previous experiments, including those of Gleason et al. (2013), at pressures greater than 50 GPa, which may be due to the lack of a pressure medium in this experiment, resulting in deviatoric stress and systematic overestimation of volumes (Meng et al. 1993). The symmetrization transition has only a subtle effect on the equation of state: the symmetric and asymmetric equations of state are nearly coincident within the symmetric high-spin stability field and there is no discontinuity in volume

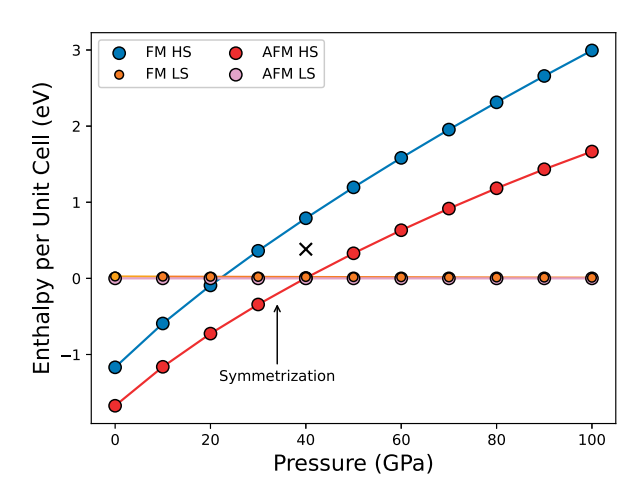


FIGURE 2. Enthalpy of FM and AFM states at static condition with respect to the AFM low-spin enthalpy. The arrow marks the pressure at which hydrogen bond symmetrization occurs, and \times marks the AFM mixed spin enthalpy.

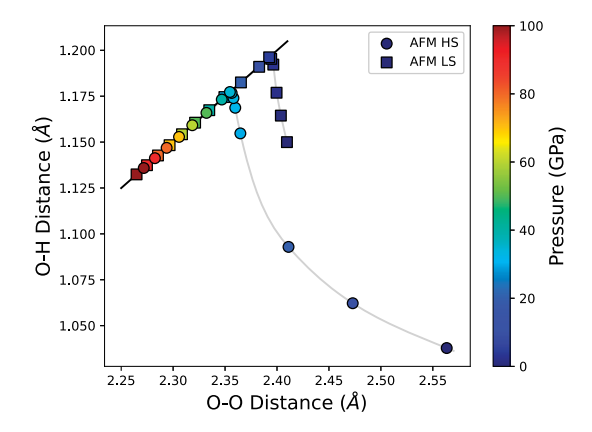


FIGURE 3. O-H vs. O-O bond distance in high-spin (circles) and low-spin (squares) states with pressure indicated by the color bar. The 2:1 line is shown in black.

at the symmetrization transition. At 300 K, the symmetrization transition occurs at 37 GPa. All subsequent results are referred to the pressure at 300 K.

Our computed crystal structures agree well with ambient structure determinations and with high-pressure measurements of the lattice parameters (Fig. 5; Table 1). We find a change in relative axial compressibilities with increasing pressure: b is the most compressible direction near ambient pressure but the stiffest at pressures exceeding 30 GPa. This change in relative compressibility is reflected in extrema in the variation of lattice parameter ratios vs. pressure, which occur at 13 GPa (b/c) and 33 GPa (a/b). The largest deviation in atomic coordinates

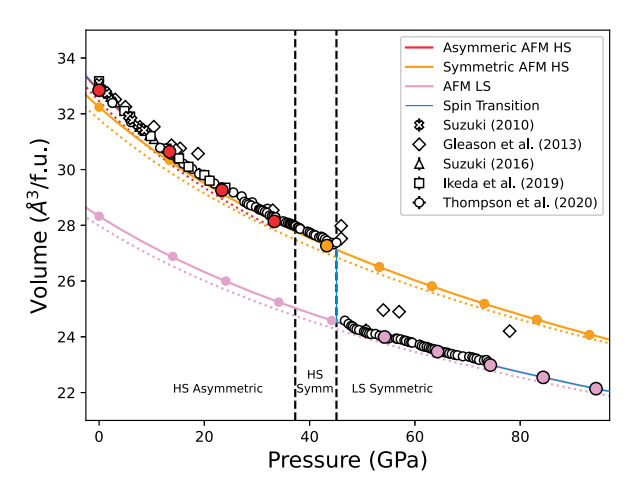
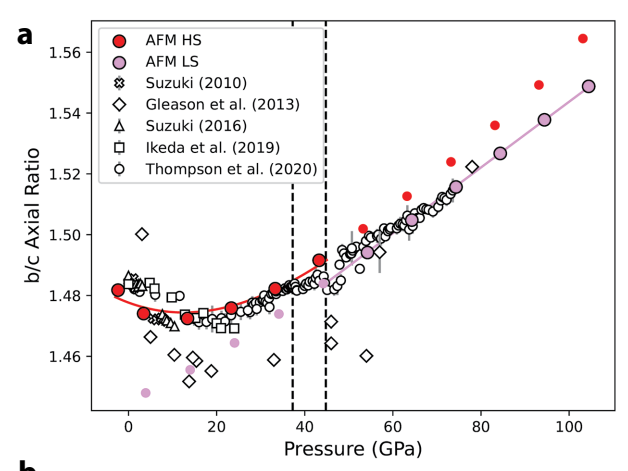


FIGURE 4. Pressure-volume equation of state for static and 300 K isotherms. Symbols in red, orange, and plum represent the asymmetric high-spin phase, the symmetric high-spin phase, and the symmetric low-spin phase at 300 K conditions. Dashed lines and solid lines represent the static and 300 K equations of state for each respective color. The blue line follows the stable phases. The vertical black dashed lines represent the hydrogen bond symmetrization and spin transition at 37 and 45 GPa, respectively, at 300 K. Equation of state fit parameters V_0 , K_0 , and K_0' are 65.68 ų, 168.55 \pm 0.30 GPa, and 3.72 \pm 0.01 for asymmetric high-spin, 64.48 ų, 193.42 \pm 0.43 GPa, and 3.51 \pm 0.02 for symmetric high-spin, and 56.65 ų, 236.56 \pm 0.42 GPa, and 3.91 \pm 0.01 for the symmetric low-spin at 300 K.



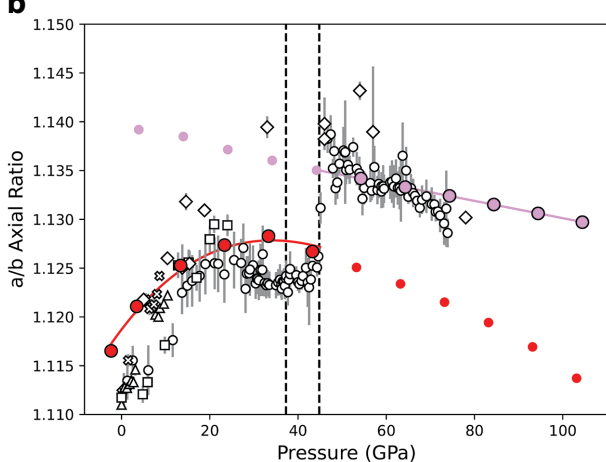


FIGURE 5. Lattice parameter ratios with respect to pressure. Red and plum represents the AFM high-spin and AFM low-spin states, respectively, and are compared to experimental results (white symbols). The vertical dashed lines represent the predicted 300 K pressure of the symmetrization transition (lower pressure) and the high-spin to low-spin transition (higher pressure).

between our results and experiment occurs for the position of the H atom, corresponding to an OH bond length of 1.02 Å for our results as compared with 0.85 Å for our experiment (Bolotina et al. 2008). Overestimation of OH bond length is expected at our level of theory (Santra et al. 2009).

The elastic moduli change discontinuously at the high-spin to low-spin transition and continuously at the symmetrization transition (Fig. 6). Because the hydrogen bonds lie within the xy-plane, the difference between asymmetric and symmetric structures is reflected more strongly in c_{11} and c_{22} than in c_{33} , and more strongly in c_{66} than in c_{44} or c_{55} . Values of c_{ijkl0} and c'_{ijkl0} show that the elastic moduli are softer and vary more rapidly with pressure in the asymmetric state as compared with the symmetric state: while the elastic moduli of the asymmetric and symmetric states become identical at the symmetrization transition, the pressure-dependence of the elastic moduli changes discontinuously at the transition. The elastic moduli are all stiffer in the low-spin state as compared with the high-spin state (Table 2). The c_{44} and c_{55} elastic moduli show a non-monotonic pressure dependence.

TABLE 1. Crystal structures of the P2 ₁ nm and Pnnm phase with respe	pect to pressure
--	------------------

Pressure	Pressure	a (Å)	<i>b</i> (Å)	c (Å)	Fe(y)	H(x)	H(y)	O1(x)	O1(y)	O2(x)	O2(y)
(Static)	(300 K)						-		-		-
					P 2₁n	m					
	O ^a	4.958	4.461	3.005	0.219	0.46	0.35	0.352	0.497	0.658	0.005
-5.88	-2.36	5.005	4.483	3.025	0.223	0.485	0.317	0.359	0.497	0.660	0.011
0	3.44	4.936	4.403	2.987	0.227	0.486	0.303	0.357	0.490	0.656	0.014
10	13.38	4.852	4.312	2.929	0.234	0.488	0.288	0.356	0.484	0.653	0.018
20	23.34	4.788	4.247	2.878	0.240	0.492	0.275	0.355	0.480	0.651	0.021
30	33.30	4.736	4.197	2.832	0.248	0.498	0.258	0.353	0.478	0.649	0.024
					Pnn	m					
40	44.19	4.692	4.164	2.792	0.25	0.5	0.25	0.351	0.476	0.648	0.024
50	54.24	4.518	3.983	2.666	0.25	0.5	0.25	0.348	0.485	0.651	0.015
60	64.29	4.493	3.965	2.635	0.25	0.5	0.25	0.347	0.484	0.652	0.016
70	74.33	4.471	3.948	2.605	0.25	0.5	0.25	0.347	0.483	0.653	0.017
80	84.37	4.450	3.933	2.576	0.25	0.5	0.25	0.346	0.483	0.654	0.017
90	94.41	4.432	3.920	2.549	0.25	0.5	0.25	0.345	0.482	0.654	0.018
100	104.44	4.414	3.908	2.523	0.25	0.5	0.25	0.345	0.481	0.655	0.019

The bulk and shear moduli increase monotonically with increasing pressure from 0 to 90 GPa, and both undergo an increase of 18% at the spin transition (Fig. 7). In the low-spin state, the shear modulus is nearly independent of pressure, reflecting, in part, the non-monotonic dependence of c_{44} and c_{55} on pressure, while c_{66} increases with increasing pressure. Our elastic constants for the low-spin state are in good agreement with previous calculations (Thompson et al. 2017), with differences (<7%) reflecting the difference in exchange-correlation functional used in the two studies (PBE vs. PBEsol in our study). We find that ε -FeOOH is highly anisotropic in both longitudinal- and shear-wave velocities at all pressures, with the shear wave velocity varying with propagation and

polarization direction by as much as 24% at zero pressure and 43% at 46 GPa.

The evolution of the hydrogen bond on compression is clearly reflected in the vibrational frequencies (Fig. 8). The frequencies of the A_1 and B_2 OH stretching modes decrease rapidly with pressure, and the bending modes increase more gradually with pressure so that the frequencies of these two branches approach each other. In the symmetrically bonded phase the OH stretching mode frequencies increase with increasing pressure, while the bending mode frequencies initially continue to increase slightly with increasing pressure. These trends are also seen in δ -AlOOH (Tsuchiya et al. 2008). The OH stretching and bending mode frequencies change little at

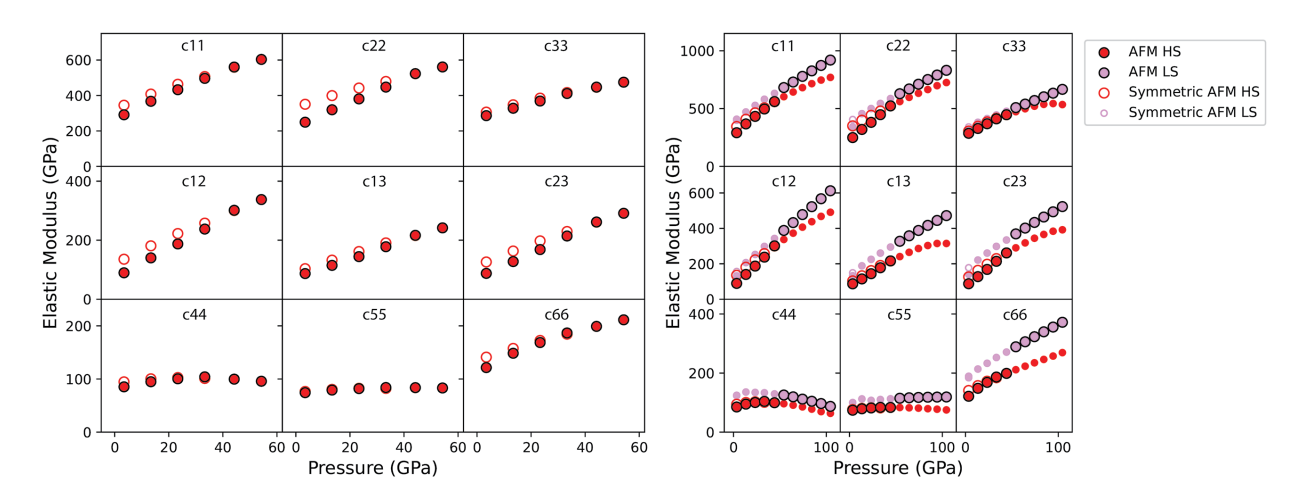


FIGURE 6. Elastic modulus with respect to pressure. Red and plum represent the AFM high-spin and AFM low-spin states, where closed and open symbols represent the asymmetric and symmetric states, respectively. Symbols representing stable phases are outlined in black.

TABLE 2. Elastic moduli c_{iiklo} and c'_{iiklo} with reference state of P = 0 GPa and T = 300 K

TABLE 2. Elastic modali cyklo with reference state of 7 = 0 of a and 7 = 500 K											
	C ₁₁	C ₁₂	C ₁₃	C ₂₂	C ₂₃	C ₃₃	C ₄₄	C ₅₅	C ₆₆		
Asymmetric HS	280(4)	78(5)	76(4)	234(6)	77(4)	272(3)	88(3)	73(1)	121(2)		
Symmetric HS	333(3)	128(2)	97(1)	335(2)	120(2)	295(1)	95(1)	74(1)	135(1)		
Symmetric LS	392(7)	147(1)	148(3)	384(2)	177(3)	319(3)	134(2)	99(2)	183(1)		
	c ' ₁₁	C' ₁₂	C' ₁₃	C'_22	C' ₂₃	C' ₃₃	C' ₄₄	C ₅₅	C' ₆₆		
Asymmetric HS	6.65(8)	4.5(1)	3.01(8)	6.6(1)	3.83(8)	4.64(6)	0.67(6)	0.59(1)	2.06(5)		
Symmetric HS	5.75(6)	3.85(5)	2.74(2)	4.99(5)	3.23(4)	4.19(2)	0.48(2)	0.51(1)	1.74(2)		
Symmetric LS	5.92(1)	4.34(1)	3.27(3)	5.22(2)	3.53(4)	4.20(4)	0.24(3)	0.62(2)	2.24(2)		

American Mineralogist, vol. 108, 2023

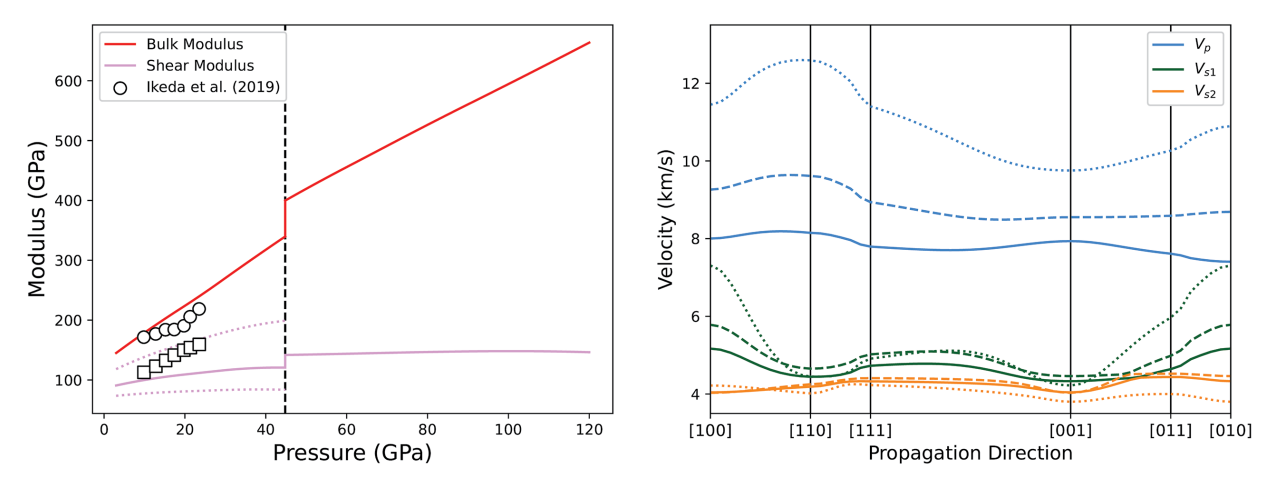


FIGURE 7. (left) Elastic properties of ε-FeOOH with respect to pressure compared with experimental measurements from Ikeda et al. (2019) (white circles and squares correspond to bulk and shear modulus, respectively). Dotted plum lines are maximum and minimum values of shear modulus from single crystal wave velocities from our results. (**right**) ν_p and ν_s dependence on propagation direction at 3.4 GPa (solid), 23.3 GPa (dashed), and 94.4 GPa (dotted).

the high-spin to low-spin transition; in the low-spin state, some of the bending mode frequencies decrease with increasing pressure. The agreement is excellent between our bending mode frequencies and experiment (Thompson et al. 2020) and our stretching mode frequencies are 1.4% smaller than the positions of peaks apparent in the experimentally reported spectrum in the OH stretching region at ambient conditions. Underestimation of OH stretching frequencies is expected at our level of theory (Santra et al. 2009).

The predicted absolute intensities of the IR- and Ramanactive modes show large changes in the vibrational spectra with increasing pressure (Fig. 9). Factor group analysis for the $P2_1nm$ and Pnnm structure shows that the irreducible representation of the zone center optic vibrations are Γ_{P2_1nm} = $7A_1(IR,R) + 4A_2(R) + 2B_1(IR,R) + 7B_2(IR,R)$ and Γ_{Pnnm} = $2B_{1u}(IR) + 5B_{2u}(IR) + 5B_{3u}(IR) + 3A_u + 2A_g(R) + 2B_{1g}(R) +$ $1B_{2g}(R) + 1B_{3g}(R)$, where IR and R denote infrared and Raman active modes. In the IR spectrum, the highest frequency peak initially increases in intensity with increasing pressure, then splits as symmetrization is approached. At a pressure that nearly coincides with symmetrization (33 GPa), the most intense peaks are no longer the highest frequency peaks, reflecting mixing of stretching and bending modes. In the low-spin state, the peak at the highest frequency becomes the one with the highest intensity again. The Raman spectrum also shows splitting of the OH highest frequency as symmetrization is approached, as well as a vanishing intensity. This decrease in intensity is expected on symmetry grounds and is also seen, for example, in H₂O (Goncharov et al. 1999).

The electronic density of states shows a finite band gap at all pressures in high-spin and low-spin states (Fig. 10). The band gap decreases with increasing pressure in both phases and increases by 0.15 eV at the high-spin to low-spin transition. The band gap is narrow and comparable to that typically seen in semiconductors: 1.9 eV at ambient pressure and 1.3 eV at the highest pressure explored in this study. Consideration of +U in our study is crucial to obtaining agreement with the experiment: if we assume that U-J = 0 eV, we find that there is no band gap at any pressure.

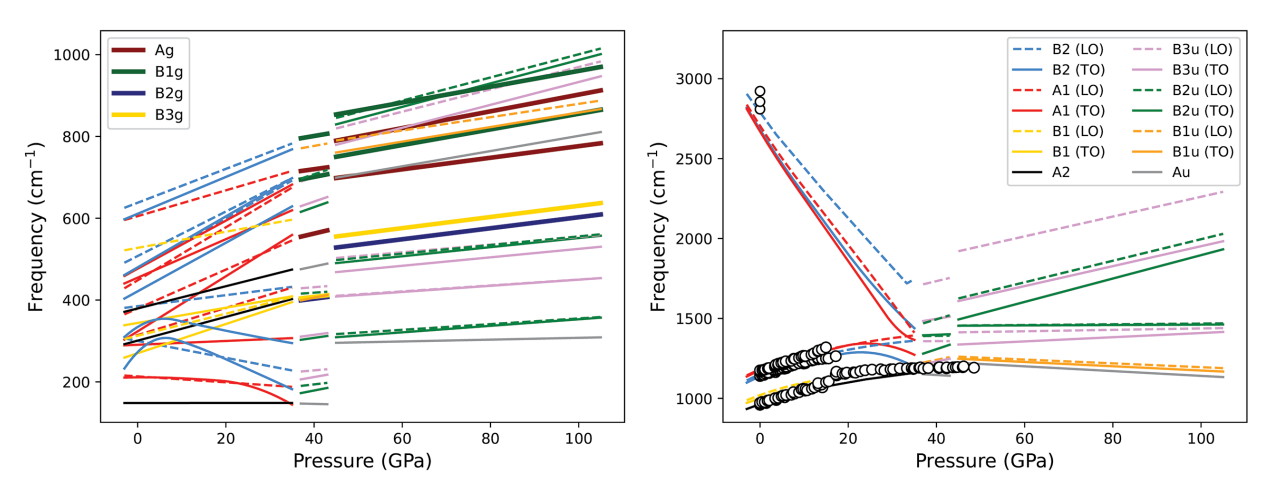
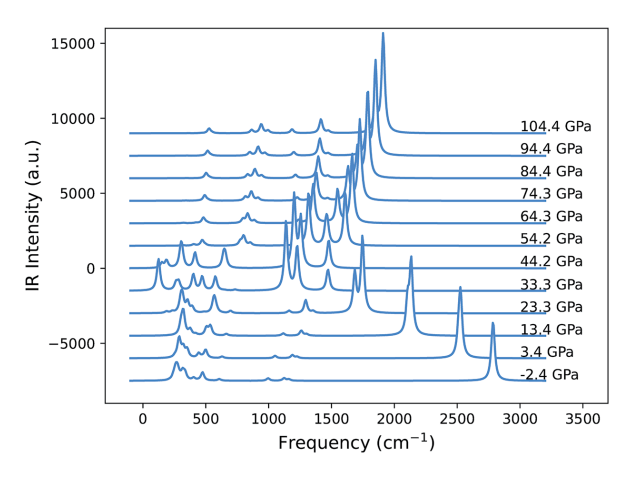


FIGURE 8. Pressure dependence of optical mode frequencies compared to experimental data in white circles (Thompson et al. 2020).

American Mineralogist, vol. 108, 2023



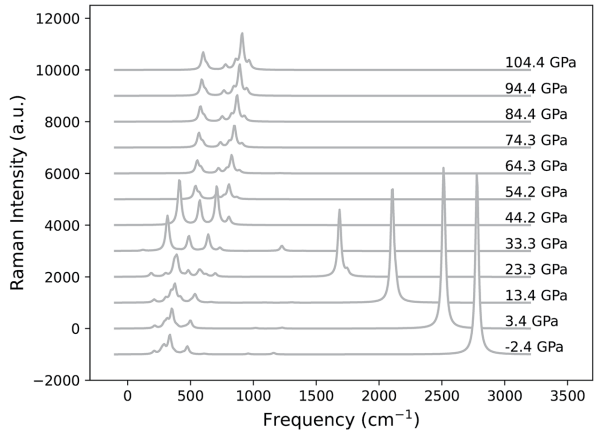


FIGURE 9. Computed IR intensities (left) and Raman intensities (right) with respect to pressure.

DISCUSSION

We find two distinct phase transitions: the symmetrization transition and the high-spin to low-spin transition, which do not coincide but are well separated in pressure, with the high-spin symmetric phase stable over a finite pressure interval (8 GPa). Our results therefore do not support the arguments of some earlier studies that symmetrization drives the high-spin to low-spin transition (Gleason et al. 2013).

Our value for the pressure of the symmetrization transition (37 GPa) is much higher than the value of 18 GPa, argued for by Thompson et al. (2020). However, Thompson et al. (2020) were not able to measure hydrogen positions and relied on other lines of evidence to argue for the pressure of symmetrization. These included the location of inflection points in the variation of lattice parameter ratios with pressure. However, we do not see inflection points but instead find local extrema (a local minimum in b/c at 13 GPa and a local maximum in a/b at 33 GPa), neither of which corresponds precisely with the pressure of hydrogen bond symmetrization. We find that the lattice parameters begin to vary nearly linearly with pressure at the symmetrization transition, a

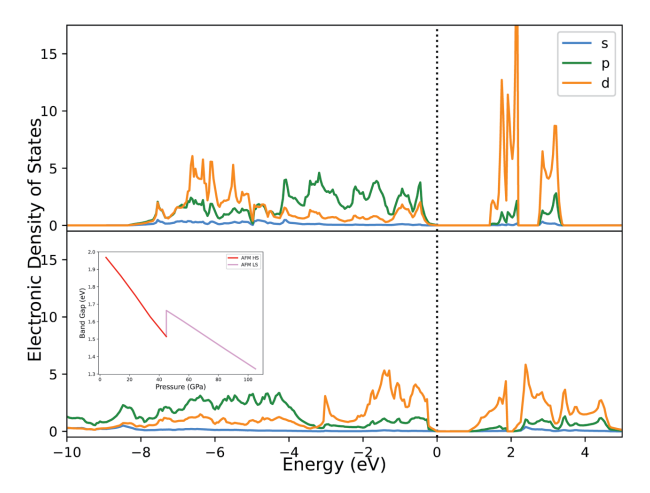


FIGURE 10. Electronic density of states at 3.4 GPa (top) and 94 GPa (bottom) with respect to s, p, and d orbitals. Inset shows the band gap dependence on pressure.

behavior also seen in a previous theoretical study of δ -AlOOH (Tsuchiya and Tsuchiya 2009).

The asymmetric to symmetric transition is continuous. The volume and bulk modulus (and all the elastic moduli) are continuous across the transition, so the transition is neither first order nor second order. Elastic wave velocities are also continuous across the symmetrization transition so that no seismological signature of the symmetrization transition is expected. Our computed vibrational spectra indicate that symmetrization might be detected via IR or Raman spectroscopy: according to our results, the symmetrization transition is characterized by changes in the pressure dependence of several modes, as well as splitting and changes in intensity. Neutron diffraction of deuterated samples, as recently done for AlOOH (Sano-Furukawa et al. 2018), could also lend further insight into symmetrization in ε-FeOOH.

Our predictions of the shear and bulk modulus of ε -FeOOH do not agree with the experimental measurements of Ikeda et al. (2019). The contrast in the pressure dependence of the shear modulus (G' = dG/dP) is particularly notable (G' = 1.2 from our results vs. G' = 4.6 from the experiment). The reason for this discrepancy is unclear. It is possible that approximations to the exchange-correlation function in our study are the cause of the discrepancy, but this seems unlikely because previous studies have found good agreement between density functional theory and experiment for the elastic moduli of δ-AlOOH (Tsuchiya and Tsuchiya 2009). The value of G' found for δ -AlOOH (1.33) is very similar to what we find for ε-FeOOH. Another possibility is that the experimental sample is textured or that the degree of the texture of the sample varied with increasing pressure. Texturing of the sample could change the shear modulus substantially because ε-FeOOH is very anisotropic, with the shear modulus varying by 24 to 43% with propagation and polarization direction at 0 and 43 GPa, respectively. ε -FeOOH is much more anisotropic than δ-AlOOH (Tsuchiya and Tsuchiya 2009).

The high-spin state is likely to remain magnetically ordered at room temperature throughout its stability field. This conclusion is based on the large enthalpy difference that we find between AFM and FM ordering. The enthalpy difference grows with increasing pressure and is similar in magnitude to the difference between the

AFM and FM ordering states of hematite [0.25 eV/Fe (Rollmann et al. 2004)], which has a Neel temperature of 950 K. We would therefore expect ε-FeOOH to have a Neel temperature of similar magnitude based on our results, in agreement with neutron diffraction experiments that show that AFM ordering exists in ε-FeOOH to at least 423 K (Pernet et al. 1975) and an estimated Neel temperature of 570 K (Pernet et al. 1973). The low-spin state is likely to be magnetically disordered at room temperature, as the difference in energy between AFM and FM order is much smaller than in the high-spin state (by a factor of ~25).

Our results suggest possible explanations for the sharpness of the high-spin to low-spin transition, as seen experimentally. The experiments of Thompson et al. (2020), show that the transition interval is irresolvably sharp and no greater than 2 GPa. This is much less than the width of the high-spin to low-spin transition at room temperature seen in other systems: for example, 10 GPa in MgSiO₃-Fe₂O₃ (Liu et al. 2018) or 18 GPa in Mg_{0.5}Fe_{0.5}O (Solomatova et al. 2016). We hypothesize that the width of the high-spin to low-spin transition in ε-FeOOH is limited by two factors. First is the presence of non-ideal interactions between high-spin and low-spin Fe cations. We find that the mixed-spin state is much higher in energy than the high-spin or low-spin states. This unfavorable energy of interaction is not included in the widely used ideal model of the spin transition (Tsuchiya et al. 2006) and has the effect of limiting the pressure interval of coexistence of high-spin and low-spin cations. Second is the presence of magnetic order. The ideal solution model, as typically applied, assumes the high-temperature limit of magnetic entropy. But this limit may not be valid in the case of ε-FeOOH because the Neel temperature of the high-spin state is likely to exceed room temperature at all pressures.

Our calculations are quasiharmonic, and we are therefore not able to explore the possibility of H disorder in ϵ -FeOOH. Consideration of H disorder is motivated by neutron diffraction experiments on δ -AlOOH, which have been interpreted to show disorder of H between two symmetrically equivalent positions along the O···O line (Sano-Furukawa et al. 2018). On the other hand, another recent study based on static structural relaxations in density functional theory and nuclear magnetic resonance experiments argues against H disorder in δ -AlOOH (Trybel et al. 2021). We suggest that molecular dynamics simulations could be used to explore the possibility of H disorder in ϵ -FeOOH.

IMPLICATIONS

The presence of ε -FeOOH in Earth's mantle could have significant effects on material properties due to the iron spintransition and hydrogen bond symmetrization. The shear modulus shows a large increase at the high-spin to low-spin transition in ε -FeOOH (an 18% increase in shear modulus, or 3% increase in shear wave velocity), behavior that contrasts with other systems. For example, in ferropericlase, the shear modulus is continuous across the high-spin to low-spin transition (Yang et al. 2015; Marquardt et al. 2018). Possible seismic detection of the high-spin to low-spin transition in the mantle has therefore focused on the effect of the transition on the bulk modulus and therefore the P-wave velocity (or bulk sound velocity) (Shephard et al. 2021). Our results show that the S-wave velocity may also be significantly affected by the spin transition in lower mantle

phases other than ferropericlase. The bulk modulus anomaly associated with the high-spin to low-spin transition is caused by the volume collapse across the pressure interval of the transition. We have assumed in the case of ϵ -FeOOH, that the high-spin to low-spin transition is sharp, consistent with the experiment, and therefore does not show any bulk modulus anomaly at room temperature, although it is possible that a narrow transition interval exists over which the bulk modulus anomaly would also exist.

Based on our results, the seismic signature of the spin transition in phase H may be more distinct than that in other systems undergoing spin transitions, including ferropericlase. In ferropericlase, the width of the transition is broader than the ideal case at all temperatures because of favorable interaction between high-spin and low-spin Fe (Holmström and Stixrude 2015), tending to mute the elastic signature of the transition. The width of the spin transition in ε-FeOOH is likely to increase with temperature. However, the unfavorable interaction between unlike spins in ε-FeOOH is likely to limit the width of the transition as seen in phase H as compared with expectations based on the ideal mixing of spin states.

Our prediction of a narrow band gap in ε-FeOOH raises the possibility that phase H may contribute to the electrical conductivity of the lower mantle as seen in electromagnetic sounding (Püthe et al. 2015). The narrow gap that we find is consistent with experimental observations of non-zero infrared transmission at all pressures measured from 23-72 GPa (Thompson et al. 2020). Moreover, the experiments show increasing absorption with increasing pressure, in agreement with the decreasing band gap with increasing pressure that we find. Our results are also consistent with experimental measurements showing that the electrical conductivity increases with increasing pressure and is small in value, typical of semiconductors (Wang and Yoshino 2021; Zhuang et al. 2022). On the other hand, the experiments show a rapid drop in transmission and a rapid increase in electrical conductivity at the high-spin to low-spin transition, whereas we find a slight increase in the band gap at the transition. Further study of the relationship between the band structure, optical absorption, and electrical conductivity is therefore warranted.

ACKNOWLEDGMENTS AND FUNDING

This project is supported by the National Science Foundation under grant EAR-1853388 to L.S. Calculations were carried out using the Hoffman2 Shared Cluster provided by UCLA Institute for Digital Research and Education's Research Technology Group.

REFERENCES CITED

Anisimov, V.I., Aryasetiawan, F., and Lichtenstein, A.I. (1997) First-principles calculations of the electronic structure and spectra of strongly correlated systems: The LDA+U method. Journal of Physics Condensed Matter, 9, 767–808, https://doi.org/10.1088/0953-8984/9/4/002.

Aoki, K., Yamawaki, H., Sakashita, M., and Fujihisa, H. (1996) Infrared absorption study of the hydrogen-bond symmetrization in ice to 110 GPa. Physical Review B: Condensed Matter, 54, 15673–15677, https://doi.org/10.1103/PhysRevB.54.15673.

Badro, J. (2014) Spin transitions in mantle minerals. Annual Review of Earth and Planetary Sciences, 42, 231–248, https://doi.org/10.1146/annurevearth-042711-105304.

Blöchl, P.E., Jepsen, O., and Andersen, O.K. (1994) Improved tetrahedron method for Brillouin-zone integrations. Physical Review B: Condensed Matter, 49, 16223–16233, https://doi.org/10.1103/PhysRevB.49.16223.

Bolotina, N.B., Molchanov, V.N., Dyuzheva, T.I., Lityagina, L.M., and Bendeliani, N.A. (2008) Single-crystal structures of high-pressure phases FeOOH, FeOOD, and GaOOH. Crystallography Reports, 53, 960–965, https://doi.org/10.1134/

- S1063774508060084.
- Chen, H., Leinenweber, K., Prakapenka, V., Prescher, C., Meng, Y., Bechtel, H., Kunz, M., and Shim, S.H. (2020) Possible H₂O storage in the crystal structure of CaSiO₃ perovskite. Physics of the Earth and Planetary Interiors, 299, 106412, https://doi.org/10.1016/j.pepi.2019.106412.
- Fu, S., Yang, J., Karato, S., Vasiliev, A., Presniakov, M.Y., Gavriliuk, A.G., Ivanova, A.G., Hauri, E.H., Okuchi, T., Purevjav, N., and others. (2019) Water concentration in single-crystal (Al,Fe)-bearing bridgmanite grown from the hydrous melt: Implications for dehydration melting at the topmost lower mantle. Geophysical Research Letters, 46, 10346–10357, https://doi.org/10.1029/2019GL084630.
- Gajdoš, M., Hummer, K., Kresse, G., Furthmüller, J., and Bechstedt, F. (2006) Linear optical properties in the projector-augmented wave methodology. Physical Review B: Condensed Matter and Materials Physics, 73, 045112, https://doi.org/10.1103/PhysRevB.73.045112.
- Giannozzi, P. and Baroni, S. (1994) Vibrational and dielectric properties of C60 from density-functional perturbation theory. The Journal of Chemical Physics, 100, 8537–8539, https://doi.org/10.1063/1.466753.
- Gleason, A.E., Jeanloz, R., and Kunz, M. (2008) Pressure-temperature stability studies of FeOOH using X-ray diffraction. American Mineralogist, 93, 1882–1885, https://doi.org/10.2138/am.2008.2942.
- Gleason, A.E., Quiroga, C.E., Suzuki, A., Pentcheva, R., and Mao, W.L. (2013) Symmetrization driven spin transition in ε-FeOOH at high pressure. Earth and Planetary Science Letters, 379, 49–55, https://doi.org/10.1016/j. epsl.2013.08.012.
- Goncharov, A.F., Struzhkin, V.V., Mao, H.K., and Hemley, R.J. (1999) Raman spectroscopy of dense H₂O and the transition to symmetric hydrogen bonds. Physical Review Letters, 83, 1998–2001, https://doi.org/10.1103/PhysRevLett.83.1998.
- Gonze, X. and Lee, C. (1997) Dynamical matrices, Born effective charges, dielectric permittivity tensors, and interatomic force constants from density-functional perturbation theory. Physical Review B: Condensed Matter, 55, 10355–10368, https://doi.org/10.1103/PhysRevB.55.10355.
- Hill, R. (1952) The elastic behaviour of a crystalline aggregate. Proceedings of the Physical Society. Section A, 65, 349–354, https://doi.org/10.1088/0370-1298/65/5/307.
- Hirschmann, M.M. (2006) Water, melting, and the deep Earth H₂O cycle. Annual Review of Earth and Planetary Sciences, 34, 629–653, https://doi.org/10.1146/ annurev.earth.34.031405.125211.
- Holmström, E. and Stixrude, L. (2015) Spin crossover in ferropericlase from first-principles molecular dynamics. Physical Review Letters, 114, 117202, https://doi.org/10.1103/PhysRevLett.114.117202.
- Holzapfel, W.B. (1972) On the symmetry of the hydrogen bonds in ice VII. The Journal of Chemical Physics, 56, 712–715, https://doi.org/10.1063/1.1677221.
- Hu, Q. and Liu, J. (2021) Deep mantle hydrogen in the pyrite-type FeO₂-FeO₂H system. Geoscience Frontiers, 12, 975–981, https://doi.org/10.1016/j.gsf.2020.04.006.
- Ikeda, O., Sakamaki, T., Ohashi, T., Goto, M., Higo, Y., and Suzuki, A. (2019) Sound velocity measurements of ε-FeOOH up to 24 GPa. Journal of Mineralogical and Petrological Sciences, 114, 155–160, https://doi.org/10.2465/jmps.181115b.
- Kresse, G. and Furthmüller, J. (1996) Efficient iterative schemes for ab initio total-energy calculations using a plane-wave basis set. Physical Review B: Condensed Matter, 54, 11169–11186, https://doi.org/10.1103/PhysRevB.54.11169.
- Kresse, G. and Joubert, D. (1999) From ultrasoft pseudopotentials to the projector augmented-wave method. Physical Review B: Condensed Matter, 59, 1758–1775, https://doi.org/10.1103/PhysRevB.59.1758.
- Le Page, Y. and Saxe, P. (2002) Symmetry-general least-squares extraction of elastic data for strained materials from ab initio calculations of stress. Physical Review B: Condensed Matter, 65, 104104, https://doi.org/10.1103/ PhysRevB.65.104104.
- Lin, J.F., Struzhkin, V.V., Jacobsen, S.D., Hu, M.Y., Chow, P., Kung, J., Liu, H., Mao, H.K., and Hemley, R.J. (2005) Spin transition of iron in magnesiowüstite in the Earth's lower mantle. Nature, 436, 377–380, https://doi.org/10.1038/ nature03825.
- Litasov, K.D. and Ohtani, E. (2007) Effect of water on the phase relations in Earth's mantle and deep water cycle. Geological Society of America. Special Paper, 421, 115–156.
- Liu, J., Lin, J.F., Mao, Z., and Prakapenka, V.B. (2014) Thermal equation of state and spin transition of magnesiosiderite at high pressure and temperature. American Mineralogist, 99, 84–93, https://doi.org/10.2138/am.2014.4553.
- Liu, J., Dorfman, S.M., Zhu, F., Li, J., Wang, Y., Zhang, D., Xiao, Y., Bi, W., and Alp, E.E. (2018) Valence and spin states of iron are invisible in Earth's lower mantle. Nature Communications, 9, 1284, https://doi.org/10.1038/s41467-018-03671-5.
- Liu, Z., Fei, H., Chen, L., McCammon, C., Wang, L., Liu, R., Wang, F., Liu, B., and Katsura, T. (2021) Bridgmanite is nearly dry at the top of the lower mantle. Earth and Planetary Science Letters, 570, 117088, https://doi.org/10.1016/j. epsl.2021.117088.
- Marquardt, H., Buchen, J., Mendez, A.S.J., Kurnosov, A., Wendt, M., Rothkirch, A., Pennicard, D., and Liermann, H.P. (2018) Elastic softening of (Mg_{0.5}Fe_{0.2})O ferropericlase across the iron spin crossover measured at seismic frequencies. Geophysical Research Letters, 45, 6862–6868, https://doi.org/

- 10.1029/2018GL077982.
- Meier, T., Petitgirard, S., Khandarkhaeva, S., and Dubrovinsky, L. (2018) Observation of nuclear quantum effects and hydrogen bond symmetrisation in high pressure ice. Nature Communications, 9, 2766, https://doi.org/10.1038/s41467-018-05164-x.
- Meng, Y., Weidner, D.J., and Fei, Y. (1993) Deviatoric stress in a quasi-hydrostatic diamond anvil cell: Effect on the volume-based pressure calibration. Geophysical Research Letters, 20, 1147–1150, https://doi.org/10.1029/93GL01400.
- Momma, K. and Izumi, F. (2008) VESTA: A three-dimensional visualization system for electronic and structural analysis. Journal of Applied Crystallography, 41, 653–658, https://doi.org/10.1107/S0021889808012016.
- Mosey, N.J., Liao, P., and Carter, E.A. (2008) Rotationally invariant ab initio evaluation of Coulomb and exchange parameters for DFT+U calculations. The Journal of Chemical Physics, 129, 014103, https://doi.org/10.1063/1.2943142.
- Musgrave, M.J.P. (1970) Crystal Acoustics: Introduction to the Study of Elastic Waves and Vibrations in Crystals, 288 p. Acoustical Society of America Holden-day.
- Nishi, M., Kuwayama, Y., Tsuchiya, J., and Tsuchiya, T. (2017) The pyrite-type high-pressure form of FeOOH. Nature, 547, 205–208, https://doi.org/10.1038/ nature22823.
- Nishi, M., Tsuchiya, J., Kuwayama, Y., Arimoto, T., Tange, Y., Higo, Y., Hatakeyama, T., and Irifune, T. (2019) Solid solution and compression behavior of hydroxides in the lower mantle. Journal of Geophysical Research. Solid Earth, 124, 10231–10239, https://doi.org/10.1029/2019JB018146.
- Ohira, I., Jackson, J.M., Solomatova, N.V., Sturhahn, W., Finkelstein, G.J., Kamada, S., Kawazoe, T., Maeda, F., Hirao, N., Nakano, S., and others. (2019) Compressional behavior and spin state of δ-(Al,Fe)OOH at high pressures. American Mineralogist, 104, 1273–1284, https://doi.org/10.2138/am-2019-6913.
- Ohira, I., Jackson, J.M., Sturhahn, W., Finkelstein, G.J., Kawazoe, T., Toellner, T.S., Suzuki, A., and Ohtani, E. (2021) The influence of δ-(Al,Fe)OOH on seismic heterogeneities in Earth's lower mantle. Scientific Reports, 11, 12036, https:// doi.org/10.1038/s41598-021-91180-9.
- Pearson, D.G., Brenker, F.E., Nestola, F., McNeill, J., Nasdala, L., Hutchison, M.T., Matveev, S., Mather, K., Silversmit, G., Schmitz, S., and others. (2014) Hydrous mantle transition zone indicated by ringwoodite included within diamond. Nature, 507, 221–224, https://doi.org/10.1038/nature13080.
- Perdew, J.P., Ruzsinszky, A., Csonka, G.I., Vydrov, O.A., Scuseria, G.E., Constantin, L.A., Zhou, X., and Burke, K. (2008) Restoring the density-gradient expansion for exchange in solids and surfaces. Physical Review Letters, 100, 136406, https://doi.org/10.1103/PhysRevLett.100.136406.
- Pernet, M., Chenavas, J., Joubert, J.C., Meyer, C., and Gros, Y. (1973) Caracterisation et Etude par effet Mössbauer d'une nouvelle variete haute pression de FeOOH. Solid State Communications, 13, 1147–1154, https://doi.org/10.1016/0038-1008/73306552-8
- Pernet, M., Joubert, J.C., and Berthet-Colominas, C. (1975) Etude par diffraction neutronique de la forme haute pression de FeOOH. Solid State Communications, 17, 1505–1510, https://doi.org/10.1016/0038-1098(75)90983-7.
- Pick, R.M., Cohen, M.H., and Martin, R.M. (1970) Microscopic theory of force constants in the adiabatic approximation. Physical Review. B, Solid State, 1, 910–920, https://doi.org/10.1103/PhysRevB.1.910.
- Püthe, C., Kuvshinov, A., Khan, A., and Olsen, N. (2015) A new model of Earth's radial conductivity structure derived from over 10 yr of satellite and observatory magnetic data. Geophysical Journal International, 203, 1864–1872, https:// doi.org/10.1093/gji/ggv407.
- Rollmann, G., Rohrbach, A., Entel, P., and Hafner, J. (2004) First-principles calculation of the structure and magnetic phases of hematite. Physical Review B: Condensed Matter and Materials Physics, 69, 165107, https://doi.org/10.1103/PhysRevB.69.165107.
- Sano-Furukawa, A., Hattori, T., Komatsu, K., Kagi, H., Nagai, T., Molaison, J.J., Dos Santos, A.M., and Tulk, C.A. (2018) Direct observation of symmetrization of hydrogen bond in δ-AlOOH under mantle conditions using neutron diffraction. Scientific Reports, 8, 15520, https://doi.org/10.1038/s41598-018-33598-2.
- Santra, B., Michaelides, A., and Scheffler, M. (2009) Coupled cluster benchmarks of water monomers and dimers extracted from density-functional theory liquid water: The importance of monomer deformations. The Journal of Chemical Physics, 131, 124509, https://doi.org/10.1063/1.3236840.
- Satta, N., Criniti, G., Kurnosov, A., Boffa Ballaran, T., Ishii, T., and Marquardt, H. (2021) High-pressure elasticity of $\delta\text{-}(Al,Fe)OOH$ single crystals and seismic detectability of hydrous MORB in the shallow lower mantle. Geophysical Research Letters, 48, 1–10, https://doi.org/10.1029/2021GL094185.
- Shephard, G.E., Houser, C., Hernlund, J.W., Valencia-Cardona, J.J., Trønnes, R.G., and Wentzcovitch, R.M. (2021) Seismological expression of the iron spin crossover in ferropericlase in the Earth's lower mantle. Nature Communications, 12, 5905, https://doi.org/10.1038/s41467-021-26115-z.
- Skelton, J.M., Burton, L.A., Jackson, A.J., Oba, F., Parker, S.C., and Walsh, A. (2017) Lattice dynamics of the tin sulphides SnS₂, SnS and Sn₂S₃: Vibrational spectra and thermal transport. Physical Chemistry Chemical Physics, 19, 12452–12465, https://doi.org/10.1039/C7CP01680H.
- Solomatova, N.V., Jackson, J.M., Sturhahn, W., Wicks, J.K., Zhao, J., Toellner, T.S., Kalkan, B., and Steinhardt, W.M. (2016) Equation of state and spin crossover

- of (Mg,Fe)O at high pressure, with implications for explaining topographic relief at the core-mantle boundary. American Mineralogist, 101, 1084–1093, https://doi.org/10.2138/am-2016-5510.
- Solomatova, N.V., Caracas, R., Bindi, L., and Asimow, P.D. (2022) Ab initio study of the structure and relative stability of MgSiO₄H₂ polymorphs at high pressures and temperatures. American Mineralogist, 107, 781–789, https://doi.org/ 10.2138/am-2021-7937.
- Stixrude, L. and Lithgow-Bertelloni, C. (2005) Thermodynamics of mantle minerals—I. Physical properties. Geophysical Journal International, 162, 610–632, https://doi.org/10.1111/j.1365-246X.2005.02642.x.
- Suzuki, A. (2010) High-pressure X-ray diffraction study of ε-FeOOH. Physics and Chemistry of Minerals, 37, 153–157, https://doi.org/10.1007/s00269-009-0319-x.
- ——— (2016) Pressure-volume-temperature equation of state of ε-FeOOH to 11 GPa and 700 K. Journal of Mineralogical and Petrological Sciences, 111, 420–424, https://doi.org/10.2465/jmps.160719c.
- ——— (2017) Thermal equation of state of goethite (α-FeOOH). High Pressure Research, 37, 193–199, https://doi.org/10.1080/08957959.2017.1301938.
- Thompson, E.C., Campbell, A.J., and Tsuchiya, J. (2017) Elasticity of ε-FeOOH: Seismic implications for Earth's lower mantle. Journal of Geophysical Research: Solid Earth, 122, 5038–5047, https://doi.org/10.1002/2017JB014168.
- Thompson, E.C., Davis, A.H., Brauser, N.M., Liu, Z., Prakapenka, V.B., and Campbell, A.J. (2020) Phase transitions in ε-FeOOH at high pressure and ambient temperature. American Mineralogist, 105, 1769–1777, https://doi.org/10.2138/am-2020-7468.
- Togo, A. and Tanaka, I. (2015) First principles phonon calculations in materials science. Scripta Materialia, 108, 1–5, https://doi.org/10.1016/j.scriptamat. 2015.07.021.
- Trybel, F., Meier, T., Wang, B., and Steinle-Neumann, G. (2021) Absence of proton tunneling during the hydrogen-bond symmetrization in. Physical Review B, 104, 104311, https://doi.org/10.1103/PhysRevB.104.104311.
- Tschauner, O., Huang, S., Greenberg, E., Prakapenka, V.B., Ma, C., Rossman, G.R., Shen, A.H., Zhang, D., Newville, M., Lanzirotti, A., and others. (2018) Ice-VII inclusions in diamonds: Evidence for aqueous fluid in Earth's deep mantle. Science, 359, 1136–1139, https://doi.org/10.1126/science.aao3030.
- Tsuchiya, J. and Mookherjee, M. (2015) Crystal structure, equation of state, and elasticity of phase H (MgSiO₄H₂) at Earth's lower mantle pressures. Scientific Reports, 5, 15534, https://doi.org/10.1038/srep15534.
- Tsuchiya, J. and Tsuchiya, T. (2009) Elastic properties of $\delta\textsc{-AlooH}$ under pressure:

- First principles investigation. Physics of the Earth and Planetary Interiors, 174, 122–127, https://doi.org/10.1016/j.pepi.2009.01.008.
- Tsuchiya, J., Tsuchiya, T., and Tsuneyuki, S. (2005) First-principles study of hydrogen bond symmetrization of phase D under high pressure. American Mineralogist, 90, 44–49, https://doi.org/10.2138/am.2005.1628.
- Tsuchiya, T., Wentzcovitch, R.M., da Silva, C.R.S., and de Gironcoli, S. (2006) Spin transition in magnesiowüstite in earth's lower mantle. Physical Review Letters, 96, 198501, https://doi.org/10.1103/PhysRevLett.96.198501.
- Tsuchiya, J., Tsuchiya, T., and Wentzcovitch, R.M. (2008) Vibrational properties of δ-AIOOH under pressure. American Mineralogist, 93, 477–482, https://doi.org/10.2138/am.2008.2627.
- Walter, M.J., Thomson, A.R., Wang, W., Lord, O.T., Ross, J., McMahon, S.C., Baron, M.A., Melekhova, E., Kleppe, A.K., and Kohn, S.C. (2015) The stability of hydrous silicates in Earth's lower mantle: Experimental constraints from the systems MgO-SiO₂–H₂O and MgO-Al₂O₃-SiO₂–H₂O. Chemical Geology, 418, 16–29, https://doi.org/10.1016/j.chemgeo.2015.05.001.
- Wang, R. and Yoshino, T. (2021) Electrical conductivity of diaspore, δ-AlOOH and ε-FeOOH. American Mineralogist, 106, 774–781, https://doi.org/10.2138/ am-2021-7605.
- Wilson, E.B. Jr., Decius, J.C., and Cross, P.C. (1980) Molecular Vibrations: The Theory of Infrared and Raman Vibrational Spectra, 416 p. Dover Publications.
- Xu, W., Greenberg, E., Rozenberg, G.Kh., Pasternak, M.P., Bykova, E., Boffa-Ballaran, T., Dubrovinsky, L., Prakapenka, V., Hanfland, M., Vekilova, O.Y., and others. (2013) Pressure-induced hydrogen bond symmetrization in iron oxyhydroxide. Physical Review Letters, 111, 175501, https://doi.org/10.1103/PhysRevLett.111.175501.
- Yang, J., Tong, X., Lin, J.F., Okuchi, T., and Tomioka, N. (2015) Elasticity of ferropericlase across the spin crossover in the Earth's lower mantle. Scientific Reports, 5, 17188, https://doi.org/10.1038/srep17188.
- Zhuang, Y., Gan, B., Cui, Z., Tang, R., Tao, R., Hou, M., Jiang, G., Popescu, C., Garbarino, G., Zhang, Y., and others. (2022) Mid-mantle water transportation implied by the electrical and seismic properties of ε-FeOOH. Science Bulletin, 67, 748–754, https://doi.org/10.1016/j.scib.2021.12.002.

Manuscript received October 13, 2022 Manuscript accepted February 4, 2023 Accepted Manuscript online February 16, 2023 Manuscript Handled By Susannah Dorfman